

First-principles calculation of lattice thermal conductivities of α -, β -, and γ - Si_3N_4

Kazuyoshi Tatsumi,^{1,2,*} Atsushi Togo,² and Isao Tanaka^{2,3,4}

¹*Institute of Materials and Systems for Sustainability,
Nagoya University, Chikusa, Nagoya 464-8603, Japan*

²*Center for Elements Strategy Initiative for Structural Materials,
Kyoto University, Sakyo, Kyoto 606-8501, Japan*

³*Department of Materials Science and Engineering,
Kyoto University, Sakyo, Kyoto 606-8501, Japan*

⁴*Nanostructures Research Laboratory, Japan Fine Ceramics Center, Atsuta, Nagoya 456-8587, Japan*

Lattice thermal conductivities of α -, β - and γ - Si_3N_4 single crystals are investigated from *ab-initio* anharmonic lattice dynamics, within the single-mode relaxation-time approximation of the linearized phonon Boltzmann transport equation. At 300 K, the lattice thermal conductivity of β - Si_3N_4 is calculated as $\kappa_{xx} = 73$ and $\kappa_{zz} = 198$ (in units of $\text{Wm}^{-1}\text{K}^{-1}$), that is consistent with the reported experimental values of 69 and 180, respectively. For α - Si_3N_4 , $\kappa_{xx} = 69$ and $\kappa_{zz} = 99$ are obtained. The difference of anisotropy between these phases is originated from their characteristic difference in the phonon band structures, closely connected to the crystal structures, specifically, the stacking orders of equivalent basal layer structures. In α - Si_3N_4 , acoustic-mode phonons below 6 THz are the main heat carriers. In β - Si_3N_4 , the phonon modes up to 12 THz contribute to the lattice thermal conductivity. In γ - Si_3N_4 , $\kappa = 81$ is obtained. The distribution of phonon mode contributions to lattice thermal conductivity with respect to phonon frequency is found to closely resemble that for κ_{xx} of β - Si_3N_4 although the phonon lifetimes of γ - Si_3N_4 are twice shorter than those of β - Si_3N_4 .

I. INTRODUCTION

Several nitride insulators are known to exhibit high thermal conductivities and are important for heat transfer materials at elevated temperatures. For example, Slack *et al.*¹ reported that wurtzite-type AlN has thermal conductivity exceeding $100 \text{ Wm}^{-1}\text{K}^{-1}$. Si_3N_4 has become another promising thermal conductive insulator because its thermal conductivity has been improved up to $177 \text{ Wm}^{-1}\text{K}^{-1}$ by using the advanced ceramic technologies related to the densification and microstructure control.^{2–5} Since the Si_3N_4 ceramics also exhibit high mechanical strength at elevated temperatures, they are regarded as ideal materials for the use in various applications, such as engine components, gas turbines, and heat sink substrates of power semiconductor devices.

At atmospheric pressure, Si_3N_4 exists in one of two phases, α and β , which are generally considered as low- and high-temperature phases, respectively.^{2,5,6} Their crystal structures belong to the space groups of P31c and P6₃/m, respectively.^{7,8} These structures have different stacking orders of equivalent basal layer structures composed of SiN_4 tetrahedra.⁹ In Fig. 1 these layer structures are depicted from the principal direction. They are denoted as A, B, C, and D in the α phase and A and B in the β phase, respectively. The stacking manners in α - and β - Si_3N_4 are thus as ABCDABCD.. and ABAB.., respectively. The α phase has additional two layer structures of C and D, which are related to A and B by the c glide operation.⁹ Along this direction the lattice constant of the α phase is approximately twice longer than that of the β phase.

The experimental thermal conductivities^{2–5,11} of the Si_3N_4 polymorphs were measured on the polycrystalline bulk samples. These values were significantly affected by

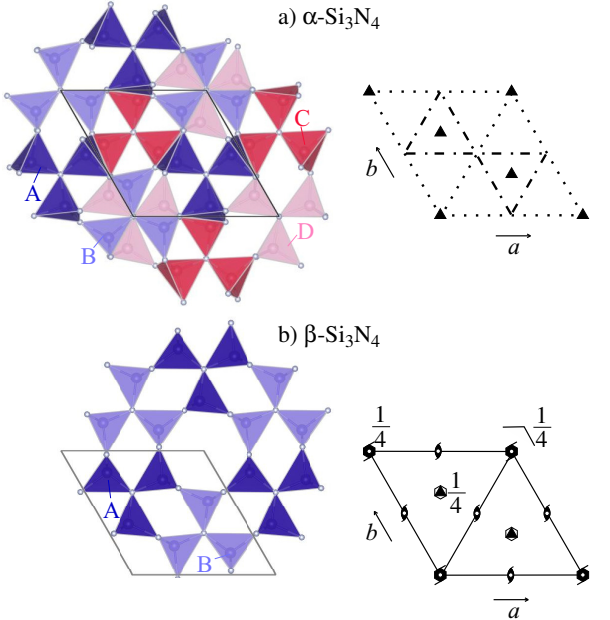


FIG. 1. (color online) Crystal structures of α - and β - Si_3N_4 . Stacking of SiN_4 tetrahedron layers are shown in left. (a) ABCDABCD.. for α - Si_3N_4 . (b) ABAB.. for β - Si_3N_4 . Space group diagrams¹⁰ in P31c (α - Si_3N_4) and P6₃/m (β - Si_3N_4) are shown in right.

the lattice defects, impurities, shapes and orientations of the constituent crystal grains;¹² the thermal conductivities intrinsic to the defect-free single crystals have not been established. As an experimental approach for them, Li *et al.*¹³ applied the high-resolution thermoreflectance microscopy on single β - Si_3N_4 grains in a ceramic sample. Their analyzed thermal conductivity was 69 and 180

$\text{Wm}^{-1}\text{K}^{-1}$ along the a and c axes, respectively. These values respectively correspond to the xx and zz elements of the lattice thermal conductivity tensor κ . We consider the anisotropy of $\kappa_{zz}/\kappa_{xx} \sim 3$ is relatively large. Theoretically, Hirosaki *et al.*¹² estimated the κ by applying the Green-Kubo formulation to the molecular dynamics (MD) method with the interatomic potentials proposed by Vashishta *et al.*¹⁴. They calculated κ_{xx} and κ_{zz} of $\alpha\text{-Si}_3\text{N}_4$ as 105 and $225 \text{ Wm}^{-1}\text{K}^{-1}$, and those of $\beta\text{-Si}_3\text{N}_4$ as 170 and $450 \text{ Wm}^{-1}\text{K}^{-1}$, respectively. The ratio κ_{zz}/κ_{xx} in $\beta\text{-Si}_3\text{N}_4$ agreed well with the experimental ratio: The κ_{ii} values overestimated the experimental values more than twice.

Based on a first principles calculation and Boltzmann transport theory¹⁵, Togo *et al.* recently calculated κ of many polymorphs of the wurtzite- and zincblende-type structures. Their crystal structures have stacking orders of the densest atom planes as ABCABC.. and ABAB.., respectively. The different stacking orders merely altered the κ .¹⁵ The phonon linewidth distribution and phonon density of states were merely altered as well.¹⁵ On the other hand, the previous MD results on α - and $\beta\text{-Si}_3\text{N}_4$ presented that the different stacking orders in these phases altered the κ largely. This has not been explained through their phonon properties. It is interesting to investigate it using the first principles anharmonic phonon calculation.

In addition to the α and β phases, a cubic spinel phase ($\gamma\text{-Si}_3\text{N}_4$) is known to form upon compression and in-situ heating.^{16,17} The reported transition pressures are scattered from 10 to 36 GPa depending on the experimental conditions.¹⁸ The γ phase is experimentally quenched to atmospheric pressure and room temperature. Its thermal conductivity has not been experimentally reported; it has been estimated only by the Slack model.¹⁹

The present study aims to qualitatively understand the lattice thermal conductivity tensors among the three Si_3N_4 phases by means of the first principles approach. We calculate the κ of the γ phase as well, for systematic understanding. After the methodology section, we examine the validity of the present results first. Our calculated thermal properties are compared with the available experimental and theoretical references. Then we investigate the characteristic behaviors of the κ in detail on the basis of the phonon band structures and phonon linewidths.

II. COMPUTATIONAL PROCEDURES

A. Lattice thermal conductivity calculation

The lattice thermal conductivities were calculated by solving the linearized Boltzmann transport equation (LBTE) within the single-mode relaxation time approximation (single-mode RTA). We also tried the direct solution of LBTE²⁰ and leave its calculated κ values in the following section. The differences between the κ cal-

culated by the single-mode RTA and the direct solution were found minor for our discussion. Therefore we limited our research to use the single-mode RTA to take advantage of its intuitive closed form of κ .

In the following sections, we denote a phonon mode by $\lambda = (\mathbf{q}, p)$ with the set of the phonon wave vector \mathbf{q} and band index p and $-\lambda \equiv (-\mathbf{q}, p)$. The relaxation time due to phonon-phonon scattering was obtained as reciprocal of linewidth, $\tau_{\lambda, \text{ph-ph}} = (2\Gamma_{\lambda})^{-1}$, where the linewidth that we employed in this study is as follows:

$$\begin{aligned} \Gamma_{\lambda} = & \frac{18\pi}{\hbar^2} \sum_{\lambda' \lambda''} |\Phi_{-\lambda \lambda' \lambda''}|^2 \times \\ & \{(n_{\lambda'} + n_{\lambda''} + 1)\delta(\omega_{\lambda} - \omega_{\lambda'} - \omega_{\lambda''}) + \\ & (n_{\lambda'} - n_{\lambda''})[\delta(\omega_{\lambda} + \omega_{\lambda'} - \omega_{\lambda''}) - \delta(\omega_{\lambda} - \omega_{\lambda'} + \omega_{\lambda''})]\}. \end{aligned} \quad (1)$$

Here ω_{λ} is the harmonic phonon frequency of the phonon mode λ , $n_{\lambda} = [\exp(\hbar\omega_{\lambda}/k_B T) - 1]^{-1}$ is the Bose-Einstein distribution at temperature T , and $\Phi_{\lambda \lambda' \lambda''}$ denotes the three-phonon-scattering strength. $\Phi_{\lambda \lambda' \lambda''}$ was obtained by usual coordinate transformation of third-order force constants from direct space to phonon space.¹⁵ The second- and third-order real-space force constants were obtained from the *ab-initio* calculation, whose details are written in the next section.

In order to compare the more realistic results of the calculated κ with the experimental thermal conductivities, the isotopic scattering effect due to the natural isotope distribution was taken into account according to the second-order perturbation theory.²¹ With the relaxation times of the phonon-phonon scattering and isotopic scattering, $\tau_{\lambda, \text{ph-ph}}$ and $\tau_{\lambda, \text{iso}}$, the total relaxation time for a phonon mode was assumed to be $1/\tau_{\lambda} = 1/\tau_{\lambda, \text{ph-ph}} + 1/\tau_{\lambda, \text{iso}}$, according to Matthiessen's rule.

The available experimental thermal conductivities in the Si_3N_4 system were measured on the polycrystalline samples and not measured from any single crystals. The conductivities measured at a polycrystalline area were affected by various lattice defects within it, such as grain boundaries, impurities, and vacancies, we crudely took them into account by a relaxation time $\tau_{\lambda, \text{bs}} = L/|\mathbf{v}_{\lambda}|$ of a phonon boundary scattering model, where $\mathbf{v}_{\lambda} = \nabla_{\mathbf{q}}\omega_{\lambda}$ is the group velocity and L a parameter regarding to the boundary mean free path. We consider $\tau_{\lambda, \text{bs}}$ as a variable parameter. We include it to κ according to Matthiessen's rule, when we compare them with those experimental conductivities.

The closed form of κ within RTA was obtained via

$$\kappa(T) = \frac{1}{N_{\mathbf{q}}\Omega} \sum_{\lambda} \tau_{\lambda}(T) \mathbf{v}_{\lambda} \otimes \mathbf{v}_{\lambda} c_{\lambda}(T), \quad (2)$$

where $N_{\mathbf{q}}$ is the number of \mathbf{q} -points, Ω is the unit cell volume, and c_{λ} is the mode heat capacity. To analyze κ in

detail, we calculate the cumulative thermal conductivity:

$$\kappa^c(\omega) = \frac{1}{N_{\mathbf{q}}\Omega} \int_0^\omega \sum_\lambda \tau_\lambda(T) \mathbf{v}_\lambda \otimes \mathbf{v}_\lambda c_\lambda(T) \delta(\omega' - \omega) d\omega', \quad (3)$$

and its derivative $\frac{\partial \kappa^c(\omega)}{\partial \omega}$ to see the phonon mode contributions to κ .

The lattice thermal conductivities were calculated with the phonon-phonon interaction calculation code PHONO3PY¹⁵, while the harmonic phonon states were analyzed with the phonon calculation code PHONOPY²².

B. Computational details

The force constants were calculated using the first-principles projector augmented wave method²³ (VASP code^{24–26}). The generalized gradient approximation (GGA) parameterized by Perdew, Burke, and Ernzerhof²⁷ was used for the exchange correlation potential. A plane wave energy cutoff of 500 eV was employed. The crystal structures were optimized until the residual forces acting on the constituent atoms were less than 10^{-6} eV/Å. The structural optimization was firstly performed for a temperature of 0 K and 0 GPa. Here the temperature and pressure were considered only for the electronic system and the zero point lattice vibration was not taken into account. The calculated lattice parameters were $a = 7.808$ Å and $c = 5.659$ Å for the α phase, $a = 7.660$ Å and $c = 2.925$ Å for the β phase, and $a = 7.787$ Å for the γ phase, which agree with the experimental data^{7,8,28} within $+0.7\%$ errors. The lattice volume optimized with the local density approximation (LDA)²⁹ for the exchange correlation potential was, for β -Si₃N₄, 3 % smaller than with GGA, which is a typical volume contraction of LDA. The κ calculated with LDA was larger by 2.6 % than with GGA. For our discussion, this difference is enough small, therefore the impact of choice of exchange correlation potential is considered to be minor in our study.

The force constants were calculated by the finite difference approach³⁰. For this calculation, we adopted the following supercells: The $1 \times 1 \times 2$, $1 \times 1 \times 3$, and $1 \times 1 \times 1$ supercells of the conventional unit cells for the third-order force constants of α , β , and γ -Si₃N₄, respectively, and the $3 \times 3 \times 4$, $3 \times 3 \times 8$ and $2 \times 2 \times 2$ for the second-order force constants. The length of the induced atomic displacement was set to 0.03 Å. Table I shows the κ calculated with several different sets of the supercells, indicating that our calculated κ is reasonably converging with respect to the size of the supercells.

Uniform \mathbf{k} -point sampling meshes of $4 \times 4 \times 2$, $4 \times 4 \times 3$, and $3 \times 3 \times 3$ were used for the third-order force constants of the α , β , and γ phases. For the α and β phases the center of the a^*b^* plane was sampled while the center on the c^* -axis was not. For the γ phase, non- Γ center mesh

TABLE I. Calculated lattice thermal conductivities of α -, β -, and γ -Si₃N₄ (WK⁻¹m⁻¹) at 300 K with respect to several combinations of supercell sizes.

Phase	Supercell (# of atoms)		LTC	
	3 rd force constants	2 nd force constants	xx	zz
α	1 \times 1 \times 1 (28)	1 \times 1 \times 1 (28)	37	57
	1 \times 1 \times 2 (56)	1 \times 1 \times 2 (56)	41	79
	1 \times 1 \times 1 (28)	2 \times 2 \times 2 (224)	55	81
	1 \times 1 \times 2 (56)	2 \times 2 \times 2 (224)	67	95
	1 \times 1 \times 2 (56)	2 \times 2 \times 3 (336)	68	97
β	1 \times 1 \times 2 (56)	3 \times 3 \times 4 (1008)	68	100
	1 \times 1 \times 2 (28)	1 \times 1 \times 2 (28)	44	173
	1 \times 1 \times 2 (28)	2 \times 2 \times 4 (224)	76	208
	1 \times 1 \times 3 (42)	2 \times 2 \times 4 (224)	71	194
	1 \times 1 \times 3 (42)	2 \times 2 \times 5 (280)	72	196
γ	1 \times 1 \times 3 (42)	3 \times 3 \times 8 (1008)	73	199
	1 \times 1 \times 1 (56)	1 \times 1 \times 1 (56)	72	
	1 \times 1 \times 1 (56)	2 \times 2 \times 2 (448)	77	
	1 \times 1 \times 1 (56)	3 \times 3 \times 3 (56)	79	

was used. For the second-order force constants, the Γ -point was only sampled for the α and β phase and the only one $\mathbf{k} = (0.5, 0.5, 0.5)$ point was sampled for the γ phase. The \mathbf{q} -point sampling meshes of $10 \times 10 \times 14$, $10 \times 10 \times 26$, and $12 \times 12 \times 12$ were used to calculate κ in Eq. (2) for the α , β , and γ phases.

Non-analytical term correction³¹ was applied to the second-order force constants to take into account the long range Coulomb forces present in ionic crystals. For the correction, static dielectric constants and Born effective charges were calculated by using the density functional perturbation theory (DFPT) as implemented in the VASP code^{32,33}.

We examined the effect of thermal expansion on κ . For this, we calculated the κ with the crystal structures which were optimized for several finite temperatures within the quasi-harmonic approximation (QHA)³⁴. These κ were different from the κ for the corresponding temperatures, calculated with the structure which was initially optimized for 0 K. We consider these differences as the effect of thermal expansion. We calculated the differences between the β -Si₃N₄ structures for $T=300, 600, 900, 1200$, and, 1500 K. The differences were found within 1 %, similar to the case of Si and Ge³⁵. For the present study, these differences are negligible and we adopt the κ calculated with the structure which was initially optimized for 0 K.

In addition, we calculated the volumetric thermal expansion coefficients. Their comparison with the experimental coefficients is useful to validate the present thermal conductivity calculation, because the thermal expansion is originated from the anharmonicity of the interatomic potential as well as κ . The calculated coefficients of the α and β phases were 4.31×10^{-6} and

$4.19 \times 10^{-6} \text{ K}^{-1}$ for 300 K, while the experimental values³⁶ are 3.75×10^{-6} and $3.55 \times 10^{-6} \text{ K}^{-1}$. The calculation reproduced the experimental tendency where the α phase has a slightly larger thermal expansion coefficient than the β phase. This supports that the present calculation enables us to qualitatively compare the calculated κ among the Si_3N_4 phases.

In order to compare the microscopic phonon properties among the three phases at the same conditions, those results calculated at 0 GPa are shown and discussed. For the γ phase, this means that we assume the condition of a virtually quenched γ phase at 0 GPa from the high pressure. To examine the analytical continuity of the properties with respect to pressures, we calculated κ of the γ phase at 10, 20, and 40 GPa as shown in Fig. 9. The phenomenological behaviour of linear dependence of κ with respect to pressure was reproduced as similar to Ref. 37. The slope was $2.89 \text{ Wm}^{-1}\text{K}^{-1}\text{GPa}^{-1}$ for the γ phase. By this dependence, we consider that the microscopic values are also varied smoothly with the pressure and those at 0 GPa are valuable to compare with the α and β phases.

C. Direct solution of LBTE

The merit to employ the single-mode RTA for thermal conductivity calculation is the closed form, by which we can intuitively understand the qualitative character of κ in terms of the relaxation time and group velocity. The microscopic understanding of the full solution of LBTE is still under the development³⁸ and the microscopic picture based on collective phonons³⁹ will require more complicated investigation.

It is known that the single-mode RTA solution of LBTE often underestimates the full solution.^{35,40} To check the underestimation, we calculated κ of the α and β phases by a direct solution of LBTE²⁰, which is one of the methods of LBTE full solutions. Their κ_{xx} and κ_{zz} without the isotope effect were 69 and $102 \text{ Wm}^{-1}\text{K}^{-1}$ for the α phase and 76 and $238 \text{ Wm}^{-1}\text{K}^{-1}$ for the β phase, respectively, while the corresponding single-mode RTA values were 70 and $102 \text{ Wm}^{-1}\text{K}^{-1}$ for the α phase and 76 and $210 \text{ Wm}^{-1}\text{K}^{-1}$ for the β phase. The κ_{zz} of the direct solution in the β phase was 13 % larger than that of the single-mode RTA solution. Since the differences in κ between the LBTE solutions are not significant, we expect the physics on those lattice thermal conductivities is well understood within the single-mode RTA in the current level of our interest. Therefore, we discuss the lattice thermal conductivities using the results of the single-mode RTA solution.

TABLE II. Calculated thermal conductivities of $\alpha\text{-Si}_3\text{N}_4$ (trigonal), $\beta\text{-Si}_3\text{N}_4$ (trigonal), and $\gamma\text{-Si}_3\text{N}_4$ (cubic) at 300 K, compared with the experimental and theoretical reference data. Theoretical bulk moduli B in units of GPa, calculated by the authors by using the present band method, are additionally presented in the fourth column.

	This work		κ	Ref. Theo.		Ref. Expt.	
	κ_{xx}	κ_{zz}		κ_{xx}	κ_{zz}	κ_{xx}	κ_{zz}
$\alpha\text{-Si}_3\text{N}_4$	68	100	224	70 ^a	105 ^b	225 ^b	- -
$\beta\text{-Si}_3\text{N}_4$	73	199	237	250 ^a	170 ^b	450 ^b	69 ^c 180 ^c
$\gamma\text{-Si}_3\text{N}_4$	77	-	296	80 ^a	- -	- -	- -

^a Ref. 19, Slack model.

^b Ref. 12, molecular dynamics (Green-Kubo).

^c Ref. 13, single crystalline grains of poly-crystals.

III. RESULTS AND DISCUSSION

A. Lattice thermal conductivities

Table II shows the present results of the κ for 300 K. $\beta\text{-Si}_3\text{N}_4$ has a markedly more anisotropic κ than $\alpha\text{-Si}_3\text{N}_4$. The directional averages $\sum_i \kappa_{ii}/3$ are 79, 115, and 77 $\text{Wm}^{-1}\text{K}^{-1}$ for the α , β , and γ phases, respectively. The value of the γ phase is similar to that of the α phase, in spite of comparatively large difference among the bulk moduli (B) that are also shown in Table II.

Table II also lists the previously reported experimental¹³ and theoretical¹² κ for the references. The theoretical results¹⁹ of the Slack model, which do not include the anisotropy in κ , are shown as κ in Table II. For the β phase, compared to the κ of the molecular dynamics¹², our κ agrees better with the experimental κ . Also, compared to the κ of the Slack model, our directional average $\sum_i \kappa_{ii}/3$ is much closer to the experimental average.

Fig. 2 shows the theoretical κ of the α and β phases as a function of T , together with the reference experimental data^{5,11}. The experimental thermal conductivities for a series of temperatures were measured from the polycrystalline sample area by the laser flash method. These thermal conductivities (denoted as $\kappa_{\text{polycrystal}}$) cannot be directly compared with the calculated intrinsic κ because they largely depended on the microstructure of the samples: They were deviated from the simple directional averages of the intrinsic κ_{ii} , depending on the shapes of the crystal grains. We treated this effect by using a parameter $0 \leq w \leq 1$ and fitting the quantities of $w\kappa_{xx} + (1-w)\kappa_{zz}$ to the experimental $\kappa_{\text{polycrystal}}$ by the least squares method. We consider these as theoretical $\kappa_{\text{polycrystal}}$.

In Fig. 2, the κ_{ii} calculated without $\tau_{\lambda,\text{bs}}$ are nearly proportional to T^{-1} because n_λ in Eq. (1) can be reduced to $\exp(-\hbar\omega_\lambda/k_B T)$. In Fig. 2-a, the experimental $\kappa_{\text{polycrystal}}$ of a chemically vapor-deposited $\alpha\text{-Si}_3\text{N}_4$ sample¹¹ is not proportional to T^{-1} and intersects the theoretical κ_{ii} . Thus no value of w adjusts the theo-

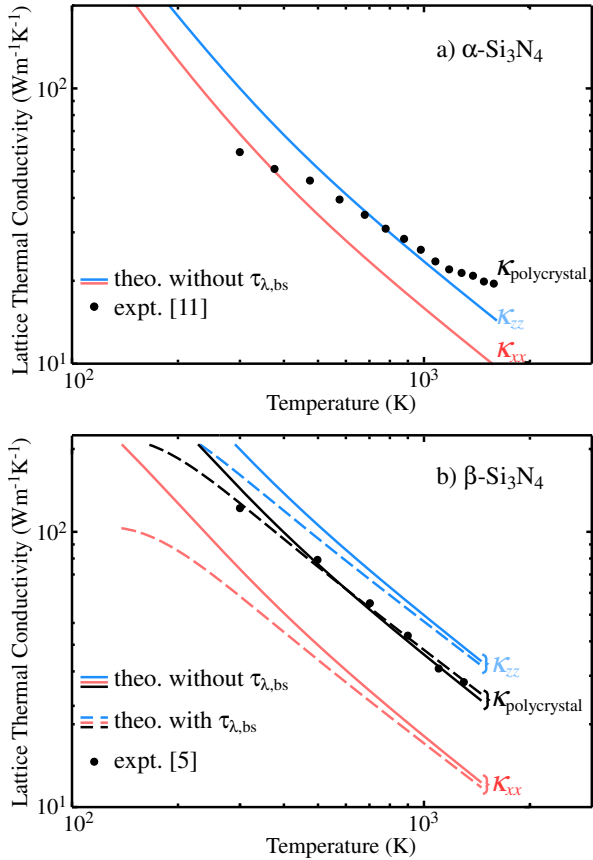


FIG. 2. (color online) Temperature dependences of thermal conductivities for α - and β -Si₃N₄. For β -Si₃N₄, theoretical conductivities with the boundary scattering effect are shown by broken lines. Theoretical $\kappa_{\text{polycrystal}}$ (see in text) for the β -Si₃N₄ sample are also shown to be compared with the experimental conductivities.

retical $\kappa_{\text{polycrystal}}$ to the experimental $\kappa_{\text{polycrystal}}$. The full solution of LBTE would negligibly cure the disagreement. Including the simple phonon lifetime of boundary scattering, $\tau_{\lambda,\text{bs}} = L/|\mathbf{v}_\lambda|$, into the total phonon lifetime according to Matthiessen's rule, could not explain the discrepancy as well. A L value of 0.6 μm , which was much smaller than the experimental grain size¹¹ of 10 μm , decreased the theoretical κ_{ii} in the low temperature side toward the experimental values, but kept the κ_{ii} in the high temperature side severely smaller than the experimental values. At present, the reason for the discrepancy between the theoretical and experimental behaviors is unclear. Although the crystal structure of the experimental sample was characterized as α -Si₃N₄, significant lattice defects existed in the sample as pointed out by Hirosaki *et al.*¹² and the simple phonon boundary scattering model may fail to describe their effects on the $\kappa_{\text{polycrystal}}$.

For the β phase, the experimental $\kappa_{\text{polycrystal}}$ are located in-between the theoretical κ_{xx} and κ_{zz} , being nearly proportional to T^{-1} . Simple directional averages

of the theoretical κ_{ii} slightly underestimate these experimental values. This is understood from the fact that the microstructure was controlled to increase the $\kappa_{\text{polycrystal}}$, and the crystalline grains were selectively grown along the c axis of the most conductive direction.⁵ The theoretical $\kappa_{\text{polycrystal}}$ were fit well with $w = 0.44$ to the experimental. For the effects of lattice defects most of which were grain boundaries, we included $\tau_{\lambda,\text{bs}}$ with $L = 0.6$ μm to further fit the theoretical curve ($w = 0.33$) to the experimental data. The L value is slightly smaller than the average grain size⁵ of 2 μm in the experiment.

B. Dispersion curves

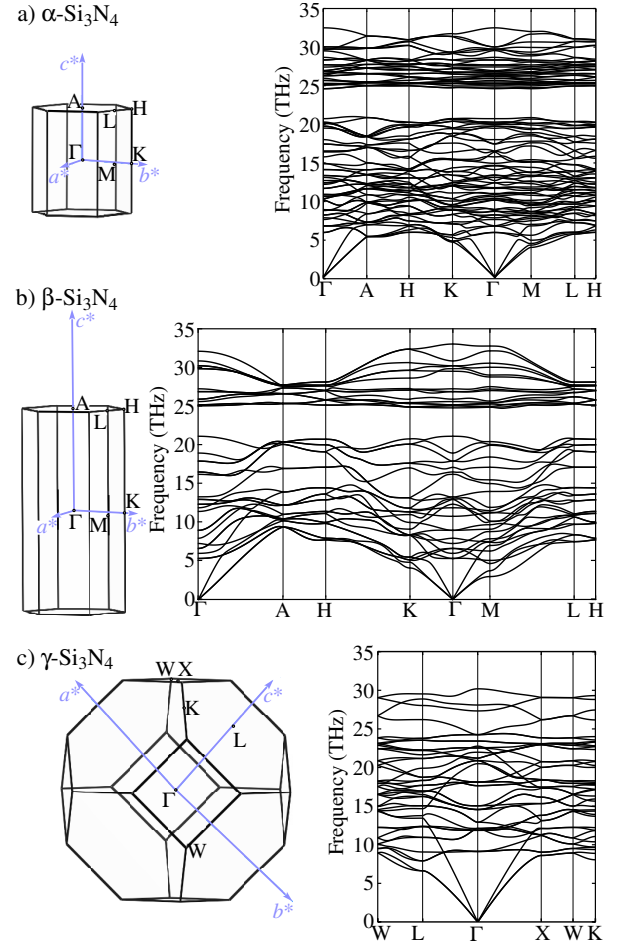


FIG. 3. (color online) Brillouin-zones (left) and calculated phonon band diagrams (right) for three Si₃N₄ phases.

Figure 3 shows the phonon band diagrams of the three Si₃N₄ phases. The entire band diagrams are almost identical to those reported earlier^{18,41}. However, here we investigate the gradients of the band dispersions, that is, the group velocities projected on the high-symmetry paths. We especially focus on their anisotropy in the α

and β phases. This was not investigated by the previous works.

In Fig.3-b, the acoustic phonon branches in the β phase increase their ω_λ much more from Γ to A than from Γ to K or Γ to M. In Fig.3-a of the α phase, the corresponding ω_λ increase similarly among these paths. This difference is due to the Γ -A path lengths. The β phase has an approximately twice longer path than the α phase; the lattice constant c of the β phase is nearly half that of the α phase, owing to the different stacking manners of the basal layer structures. The anisotropic dispersions indicate the anisotropic \mathbf{v}_λ . This will be investigated further in the following sections. Normally, optical phonon branches are flat; however, the β phase shows significantly large gradients of the band dispersions of the low frequency optical phonon branches. This indicates that the \mathbf{v}_λ of these phonon modes are large as well.

In the γ phase, the acoustic phonon branches show significant linear dispersions on the Γ -L and Γ -X paths. Their roughly constant gradients are large, reflecting the large B of the γ phase.

C. ω_λ counter map on reciprocal plane

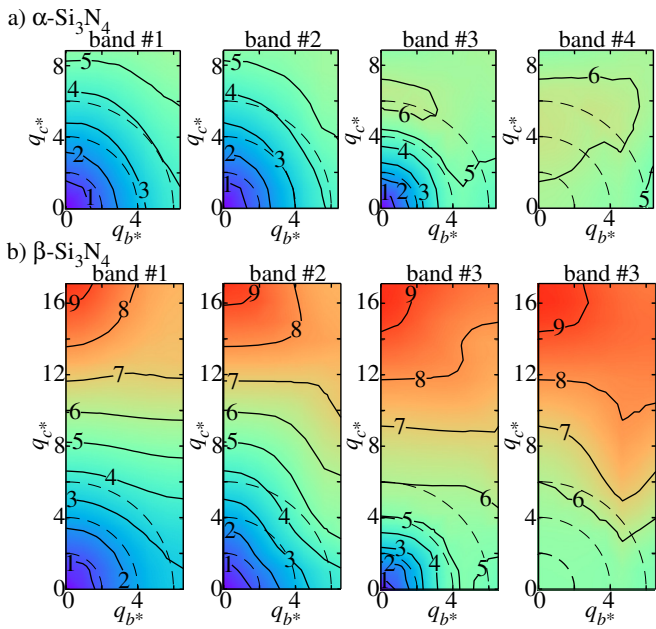


FIG. 4. (color online) Contour maps of phonon frequency (THz) on the b^*c^* planes of Brillouin-zones. The coordination in the reciprocal plane are in units of 10^{-2} \AA^{-1} . The maps for the four lowest-frequency phonon modes are shown. The frequency landscapes are formed by simply connecting the frequencies of the same band indices, assigned by ascending order of frequency at the respective \mathbf{q} points.

We investigate the anisotropy in the \mathbf{v}_λ by using another geometry, that is, a cross-section of the Brillouinzone. Fig. 4 shows counter maps of ω_λ on the b^*c^* plane.

We show the maps for the four lowest-frequency bands, because they contribute significantly to the κ . There were negligible differences between the distributions on the b^*c^* plane and the other planes containing the c^* axis. Thus we select the b^*c^* plane as a representative. In the α phase, the distributions are nearly isotropic. The \mathbf{v}_λ are thus nearly isotropic. In the β phase, the iso-frequency lines in $0.06 \leq q_{c^*} \leq 0.12 \text{ \AA}^{-1}$ are rather parallel to the q_{b^*} axis. The \mathbf{v}_λ there orient closely to the c^* axis direction. This confirms the large anisotropy in the \mathbf{v}_λ of the acoustic and low-frequency optical phonon branches in the β phase.

D. Frequency-dependences of κ^c , \mathbf{v}_λ and Γ_λ

We have investigated in the previous two sections the anisotropy in the \mathbf{v}_λ , which can explain the anisotropy in the κ . Here we more completely investigate the characteristic points in the κ by using the phonon properties existing in the closed form of RTA in Eq. (2). These properties are taken over the Brillouin zone, similar to κ . In order to investigate these properties with respect to the phonon modes, we show in Fig. 5 frequency distributions of these properties: Phonon densities of states (DOS), $g(\omega)$, shown in Fig. 5-a can be viewed as frequency distributions of heat carriers. In DOS, a low-frequency main peak is denoted by an arrow. Considering the band diagrams, this peak is approximately associated with flattening of acoustic phonon branches near Brillouin zone boundaries. In Fig. 5-b, κ^c and their first derivatives are shown in order to find the phonon mode contribution to the κ clearly. In Fig. 5-c, we show weighted DOS with the vector-direct-product of group velocities (WDOS), $\mathbf{h}(\omega)$,

$$\mathbf{h}(\omega) = \frac{1}{N_q Z} \sum_{\lambda} \mathbf{v}_{\lambda} \otimes \mathbf{v}_{\lambda} \delta(\omega - \omega_{\lambda}), \quad (4)$$

where Z is the number of formula units in the unit cell. WDOS shows the impacts of \mathbf{v}_{λ} and number of heat carriers. Phonon linewidths are a remaining important property. They are shown as scatter plots ($\Gamma_{\lambda}, \omega_{\lambda}$) in Fig. 5-d.

Among the panels in Fig. 5, the γ phase has its DOS, WDOS, and Γ_{λ} distribution much different from the others, consistently with the large differences in the crystal structure. Some of the differences are remarked as follows:

(1) The DOS peak is located at the highest frequency among the three phases. This is consistent with the band diagram showing the linear dispersions of the acoustic phonon branches with the large gradients. Reflecting this feature, in the lower frequency side of the peak, the DOS has the lowest intensities among the three phases. This means the smallest distribution of heat carriers.

(2) At most of the frequencies with phonon modes largely contributing to κ , the WDOS is the next largest to h_{zz} of the β phase. This means the large v_{λ} of the phonon modes in the acoustic phonon branches.

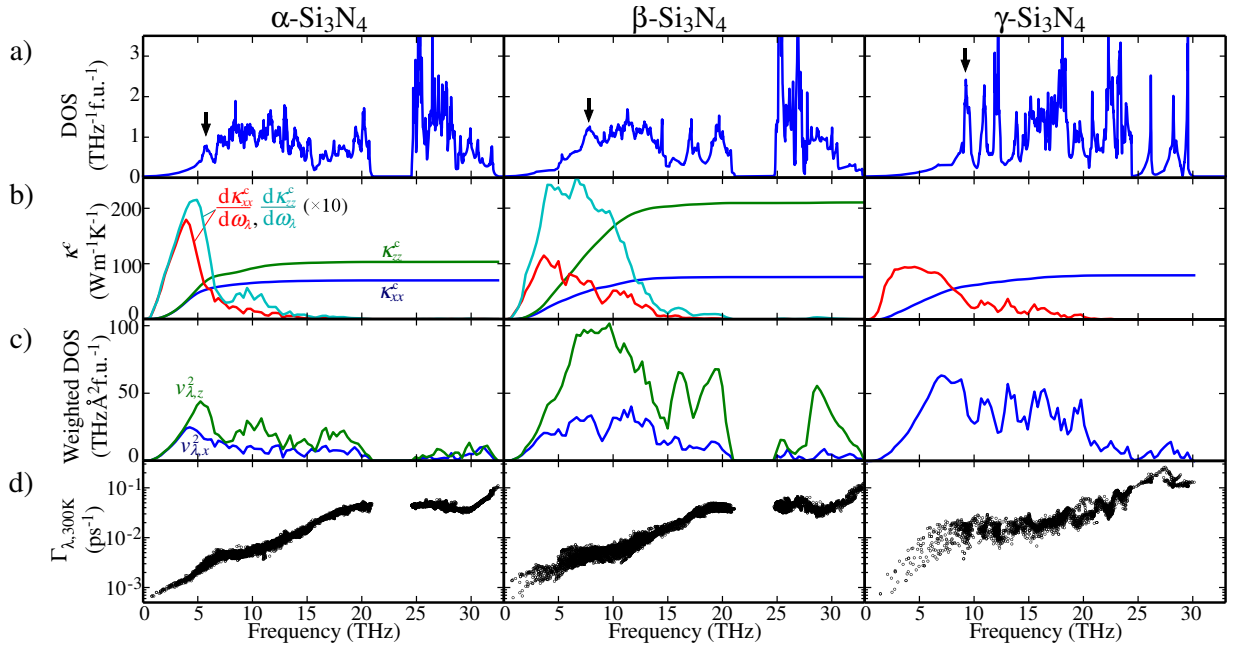


FIG. 5. (color online) Microscopic phonon properties of three Si₃N₄ phases. DOS (a), Cumulative thermal conductivity κ^c and its derivative (b), weighted DOS with $v_{\lambda,i}^2$ (c), and linewidth Γ_λ (d).

(3) At the same frequencies, the most of linewidths are larger than those of the other two phases. For this point, we refer to the $|\Phi_{\lambda\lambda'\lambda''}|^2$ included in Eq. (1). In Table. III, their averages are taken over frequency ranges of 0–15 or 0–30 THz for ω_λ and all indices in λ' and λ'' . The γ phase has the average over ω_λ in 0–15 THz much larger than that of the other phases. The large $|\Phi_{\lambda\lambda'\lambda''}|^2$ likely explain the largest linewidths. For more complete analysis, this will be further mentioned later.

In summary of (1), (2), and, (3), in spite of the large v_λ of the phonon modes in the acoustic phonon branches, owing to the large linewidths and small DOS, the κ_{xx}^c is not so large and resembles the κ_{xx}^c of the β phase.

TABLE III. Averages of $\Phi_{\lambda\lambda'\lambda''}$ over frequency ranges of ω_λ (0–15 and 0–35 THz) and all (λ', λ') . The values are in units of 10^{-10} eV²f.u.⁻¹.

Frequency Range (THz)	Phase		
	α	β	γ
0–15	2.66	2.63	5.76
0–30	13.1	13.0	11.4

We turn to compare the properties between the α and β phases. It is interesting that κ^c in the β phase still increase significantly in the higher frequency side to the DOS peak. In this frequency range, WDOS of the β phase show still large intensities. The linewidth distribution as well as DOS are similar between the two phases. Thus the large v_λ simply increase the κ^c there. The large v_λ in this frequency range are consistent with the band

diagram we have examined. In Figs. 5-b and c, the profiles of $\frac{d\kappa_{ii}^c}{d\omega_\lambda}$ are qualitatively explained by the h_{ii} with the same indices. Again, with the similar DOS and Γ_λ , the different anisotropy in the v_λ simply accounts for the different anisotropy in κ .

It is left curious that Γ_λ are similar between these two phases although v_λ show marked differences. We investigate this further. As for not linewidths but thermal conductivities, Lindsay *et al.*⁴² found that the experimental thermal conductivities were inversely proportional to the number of configurations for three phonons $\{\lambda, \lambda', \lambda''\}$ involved in the three-phonon scattering, which was referred as the phase space available for the three-phonon scattering⁴². In analogy to Lindsay *et al.*, we can say that the present linewidth depends on the number of configurations for the available two phonons, $\{\lambda', \lambda''\}$. Moreover, it also depends on $|\Phi_{\lambda\lambda'\lambda''}|^2$ as well. We examine these terms one-by-one. A distribution of two-phonon configurations is represented as a joint density of states (JDOS), $D_2(\mathbf{q}, \omega)$,

$$D_2(\mathbf{q}, \omega) = D_2^{(1)}(\mathbf{q}, \omega) + D_2^{(2)}(\mathbf{q}, \omega) \quad (5)$$

where

$$\begin{aligned} D_2^{(1)} &= \frac{1}{N} \sum_{\lambda' \lambda''} \Delta(-\mathbf{q} + \mathbf{q}' + \mathbf{q}'') \\ &\times [\delta(\omega + \omega_{\lambda'} - \omega_{\lambda''}) + \delta(\omega - \omega_{\lambda'} + \omega_{\lambda''})], \\ D_2^{(2)} &= \frac{1}{N} \sum_{\lambda' \lambda''} \Delta(-\mathbf{q} + \mathbf{q}' + \mathbf{q}'') \\ &\times \delta(\omega - \omega_{\lambda'} - \omega_{\lambda''}), \end{aligned}$$

with $\Delta(\mathbf{x})$ giving 1 if \mathbf{x} is a reciprocal lattice vector and otherwise zero. In more rigorous study, JDOS should be weighted with the Bose-Einstein distribution terms appeared in Eq. (1). We firstly employ the JDOS to intuitively examine the similarity between the Γ_λ of the α and β phases. The weighted JDOS (WJDOS) will be briefly shown later including that of the γ phase.

Fig. 6 shows frequency-functions of JDOS at several different \mathbf{q} -points. They have very weak \mathbf{q} -point dependences. At the low frequency region with the phonon modes largely contributing to the κ , among the two terms of $D_2^{(1)}$ and $D_2^{(2)}$ in Eq. (5), dominant is $D_2^{(1)}$. The $D_2^{(1)}$ basically corresponds to the half part ($\omega \geq 0$) of the auto-correlation function of the DOS. The DOS for both of the α and β phases in Fig. 5-a have a frequency gap. The $D_2^{(1)}$ reflect this DOS feature, dropping suddenly around 0 THz and showing a small shoulder around 5 THz, which corresponds to the width of the gap. Moreover the $D_2^{(1)}$ shows a broad peak around 18 THz, which corresponds to the frequency giving the largest correlation between the DOS in the higher and lower frequency portions to the gap. Because the gap is originated from the differences in the vibrations of the planer NSi_3 contained in both of the α and β crystal structures,⁴¹ the major shapes of the $D_2^{(1)}$, reflecting this gap feature, are similar in these phases. In the present Si_3N_4 system, the number of phonon modes in the acoustic and low-frequency optical phonon branches are much smaller than the total number of the other phonon modes. Therefore JDOS are mainly determined by the other phonon modes, even if the frequency is close to the ω_λ of the acoustic and low-frequency optical phonon modes.

The WJDOS of $N_2(\omega, \mathbf{q})$ are shown in Fig. 7. For the comparison among the three phases, we only show the frequency distributions at $\mathbf{q} = (0, 0, 0)$. Similar to JDOS, the \mathbf{q} dependences of the WJDOS were negligible. The terms of the two classes corresponding to $D_2^{(1)}$ and $D_2^{(2)}$ in JDOS are denoted as $N_2^{(1)}$ and $N_2^{(2)}$. The weighting factors reduce the $N_2^{(1)}$ near 0 THz and enhance the $N_2^{(2)}$ in the high frequency range. However the $N_2^{(1)}$ are dominant in the low frequency range where the phonon modes largely contribute to the κ . These $N_2^{(1)}$ have similar intensities there, having insignificant differences for the impacts on the linewidths among the three phases. As for $|\Phi_{\lambda\lambda'\lambda''}|^2$, Table. III indicates that the $|\Phi_{\lambda\lambda'\lambda''}|^2$ are similar between the α and β phases. With these similar impacts of the (W)JDOS and $|\Phi_{\lambda\lambda'\lambda''}|^2$, the linewidth distributions in Fig. 5-d of the two phases are similar. For the γ phase, the large $|\Phi_{\lambda\lambda'\lambda''}|^2$ is confirmed to attribute to the large linewidths.

Finally, a small but interesting difference in linewidth distributions are seen between the α and β phases in Fig. 5-d. Γ_λ below 5 THz are aligned on a single smooth line in the α phase, while those in the β phase are scattered roughly on two branches. This difference is investigated with directions of the atomic vibrations of the

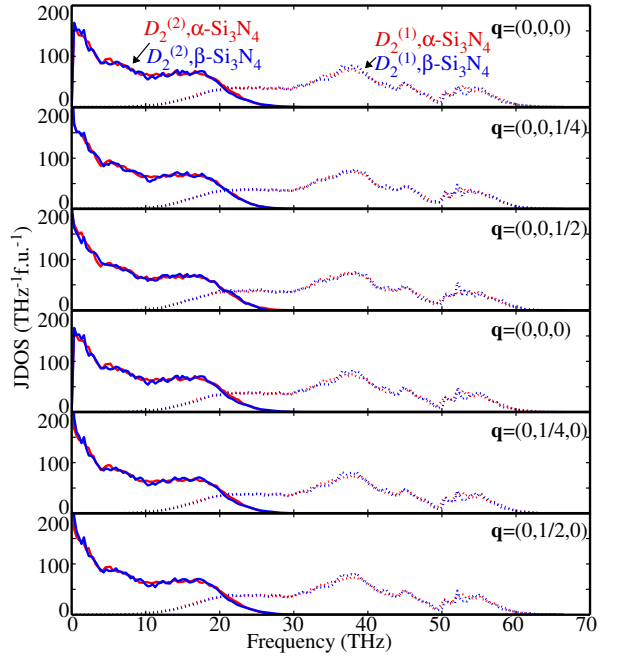


FIG. 6. (color online) JDOS of α - and β - Si_3N_4 at different \mathbf{q} points. The first and forth rows are JDOS at the same Γ -point but calculated with the polarization for non-analytic term correction set along c^* and b^* , respectively.

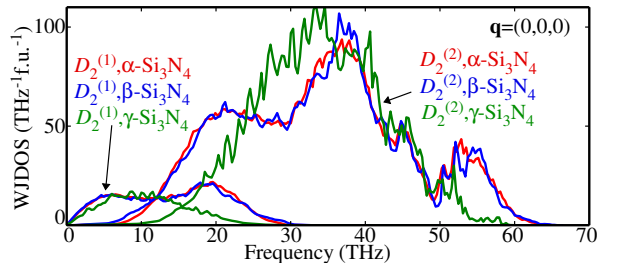


FIG. 7. (color online) Comparison of WJDOS at $\mathbf{q} = (0, 0, 0)$ for 300 K among the three phases.

phonon modes. Fig. 8 enlarges the $(\Gamma_\lambda, \omega_\lambda)$ plots in this frequency range. In Fig. 8-a, the Γ_λ are classified using colors according to the sums of the squares of the eigenvector components along the \mathbf{q} ; the sum is 1 for a perfectly longitudinal wave. However, these sums have no clear color-contrast distinguishing the two branches in the β phase. Fig. 8-b shows the same plot as Fig. 8-a, but with colors according to the sums of the squares of the eigenvector components along the ab plane, which has 1 when the eigenvectors lie on the ab plane. There is a tendency in the β phase that Γ_λ are large for vibrations along the ab plane. Therefore, within the single-mode RTA, for the phonon modes below 5 THz, all of which belong to the acoustic phonon branches, vibration modes along the ab plane are more easily scattered in the β phase, no matter whether they are longitudinal or transverse. For the panel of β - Si_3N_4 in Fig. 8-b, a straight line roughly assigns the phonon modes to the two branches.

The numbers of the phonon modes assigned to the upper and lower branches are 157 and 58, whose ratio is consistent to the population ratio of the vibration modes along and out of the ab plane.

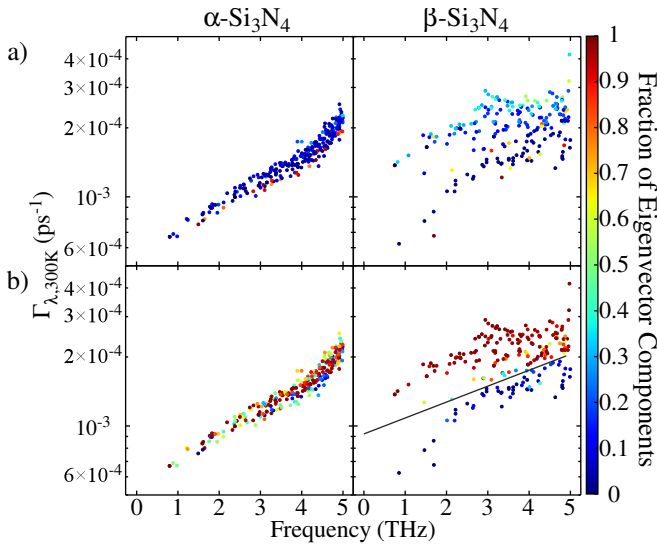


FIG. 8. (color online) Distribution of linewidths $\omega_\lambda \leq 5$ THz with colors with respect to strengths of eigenvector components along \mathbf{q} (a) and on ab plane (b).

IV. SUMMARY

In the present study, we investigate the lattice thermal conductivities of the three Si_3N_4 phases, by using the lattice dynamics based on the first principles interatomic force constants. The main remarks are as follows:

1) In the α - and β - Si_3N_4 , whose crystal structures are characterized by the stacking manners of the basal layer structures, which largely alter κ . The κ of α - Si_3N_4 is rather isotropic, while the κ_{zz} of the β phase is twice or more larger than the other κ_{ii} of the three phases.

2) In the α phase, the acoustic mode phonons below

6 THz are the main heat carriers, while in the β phase, the phonons below 12 THz contribute to the κ . The group velocities alone qualitatively explain this and the different behaviours in κ between these phases. This is partly because JDOS is insensitive to the group velocities of the phonon modes whose number is relatively small.

3) In the γ phase, the κ_{xx} is relatively small. The κ_{xx}^c is similar to that of β - Si_3N_4 . Its large $|\Phi_{\lambda\lambda'\lambda''}|^2$ and small DOS attribute to these characters.

ACKNOWLEDGMENTS

The present work was partly supported by Grants-in-Aid for Scientific Research of MEXT, Japan (Grant No. 15K14108 and ESISM (Elements Strategy Initiative for Structural Materials) of Kyoto University).

Appendix A: Pressure dependence of lattice thermal conductivity of γ -phase

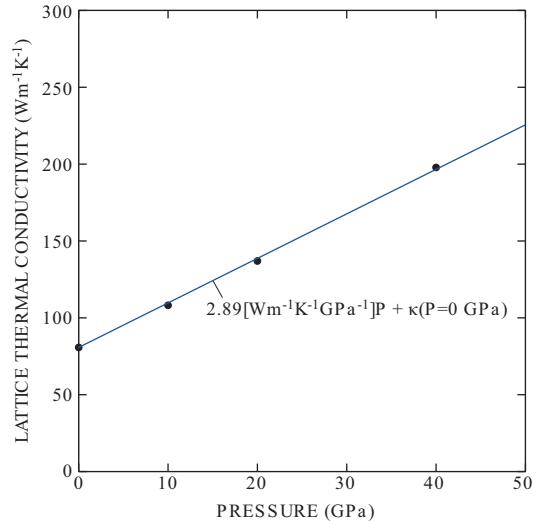


FIG. 9. (color online) Pressure dependence of lattice thermal conductivity of γ - Si_3N_4 .

* k-tatsumi@imass.nagoya-u.ac.jp

¹ G. Slack, Journal of Physics and Chemistry of Solids **34**, 321 (1973).

² Y. Zhou, H. Hyuga, D. Kusano, Y.-i. Yoshizawa, and K. Hirao, Advanced Materials **23**, 4563 (2011).

³ K. Hirao, K. Watari, H. Hayashi, and M. Kitayama, MRS Bulletin **26**, 451 (2001).

⁴ K. Watari, Journal of the Ceramic Society of Japan **109**, S7 (2001).

⁵ N. Hirosaki, Y. Okamoto, M. Ando, F. Munakata, and Y. Akimune, Journal of the Ceramic Society of Japan **104**, 49 (1996).

⁶ F. L. Riley, Journal of the American Ceramic Society **83**, 245 (2000).

⁷ M. Yashima, Y. Ando, and Y. Tabira, The Journal of Physical Chemistry B **111**, 3609 (2007).

⁸ D. Du Boulay, N. Ishizawa, T. Atake, V. Streltsov, K. Furuya, and F. Munakata, Acta Crystallographica Section B: Structural Science **60**, 388 (2004).

⁹ S. Hampshire, H. Park, D. Thompson, and K. Jack, Nature **274**, 880 (1978).

¹⁰ T. Hahn, ed., *International tables for crystallography*, Vol. A (John Wiley & Sons, Inc., 2011).

- ¹¹ T. Hirai, S. Hayashi, and K. Niihara, AM. CERAM. SOC. BULL. Am. Ceram. Soc. Bull. **57**, 1126 (1978).
- ¹² N. Hirosaki, S. Ogata, C. Kocer, H. Kitagawa, and Y. Nakamura, Physical Review B **65**, 134110 (2002).
- ¹³ B. Li, L. Pottier, J. Roger, D. Fournier, K. Watari, and K. Hirao, Journal of the european ceramic society **19**, 1631 (1999).
- ¹⁴ R. Vashishta, R. K. Kalia, A. Nakano, and I. Ebbssö, *Amorphous Insulators and Semiconductor*, edited by M. F. Thorpe and M. I. Mitkova (Kluwer, 1996).
- ¹⁵ A. Togo, L. Chaput, and I. Tanaka, Physical Review B **91**, 094306 (2015).
- ¹⁶ A. Zerr, G. Miehe, G. Serghiou, M. Schwarz, E. Kroke, R. Riedel, H. Fueß, P. Kroll, and R. Boehler, Nature **400**, 340 (1999).
- ¹⁷ Y. Zhang, A. Navrotsky, and T. Sekine, Journal of materials research **21**, 41 (2006).
- ¹⁸ B. Xu, J. Dong, P. F. McMillan, O. Shebanova, and A. Salamat, Physical Review B **84**, 014113 (2011).
- ¹⁹ D. Morelli and J. Heremans, Applied physics letters **81**, 5126 (2002).
- ²⁰ L. Chaput, Physical review letters **110**, 265506 (2013).
- ²¹ S.-i. Tamura, Physical Review B **27**, 858 (1983).
- ²² A. Togo and I. Tanaka, Scripta Materialia **108**, 1 (2015).
- ²³ P. E. Blöchl, Phys. Rev. B **50**, 17953 (1994).
- ²⁴ G. Kresse and J. Furthmüller, Physical review B **54**, 11169 (1996).
- ²⁵ G. Kresse, J. Non-Cryst. Solids **193**, 222 (1995).
- ²⁶ D. J. Kresse, Georg, Phys. Rev. B **59**, 1758 (1999).
- ²⁷ J. P. Perdew, K. Burke, and M. Ernzerhof, Phys. Rev. Lett. **77**, 3865 (1996).
- ²⁸ W. Paszkowicz, R. Minikayev, P. Piszora, M. Knapp, C. Bähtz, J. Recio, M. Marques, P. Mori-Sánchez, L. Gerward, and J. Jiang, Phys. Rev. B **69**, 052103 (2004).
- ²⁹ D. M. Ceperley and B. Alder, Physical Review Letters **45**, 566 (1980).
- ³⁰ S. Wei and M. Chou, Physical review letters **69**, 2799 (1992).
- ³¹ Y. Wang, J. Wang, W. Wang, Z. Mei, S. Shang, L. Chen, and Z. Liu, J. Phys.: Condens. Matter **22**, 202201 (2010).
- ³² M. Gajdoš, G. Hummer, G. Kresse, J. Furthmüller, and B. F. Phys. Rev. B **73**, 045112 (2006).
- ³³ X. Wu, D. Vanderbilt, and D. R. Hamann, Phys. Rev. B **72**, 035105 (2005).
- ³⁴ M. T. Dove, *Introduction to lattice dynamics*, Vol. 4 (Cambridge university press, 1993) pp. 76–77.
- ³⁵ A. Ward and D. Broido, Physical Review B **81**, 085205 (2010).
- ³⁶ R. Minikayev, W. Paszkowicz, P. Piszora, M. Knapp, and C. Bähtz, “Thermal expansion of and silicon nitride,” (2007).
- ³⁷ P. Andersson, Journal of Physics C: Solid State Physics **18**, 3943 (1985).
- ³⁸ A. Cepellotti and N. Marzari, Physical Review X **6**, 041013 (2016).
- ³⁹ R. J. Hardy, Physical Review B **2**, 1193 (1970).
- ⁴⁰ S. Mukhopadhyay, L. Lindsay, and D. J. Singh, Scientific reports **6** (2016).
- ⁴¹ A. Kuwabara, K. Matsunaga, and I. Tanaka, Physical Review B **78**, 064104 (2008).
- ⁴² L. Lindsay and D. A. Broido, J. Phys.: Condens. Matter **20**, 165209 (2008).